



## Mean flow structure in high aspect ratio microchannel flows

J.R. Elsnab<sup>a</sup>, D. Maynes<sup>b</sup>, J.C. Klewicki<sup>c</sup>, T.A. Ameel<sup>a,\*</sup>

<sup>a</sup> Department of Mechanical Engineering, University of Utah, Salt Lake City, UT 84112, USA

<sup>b</sup> Department of Mechanical Engineering, Brigham Young University, Provo, UT 84602, USA

<sup>c</sup> Department of Mechanical Engineering, University of New Hampshire, Durham, NH 03824, USA

### ARTICLE INFO

#### Article history:

Received 23 March 2010

Accepted 24 March 2010

#### Keywords:

MTV  
Laminar  
Transitional  
Turbulent  
Microscale

### ABSTRACT

An experimental investigation of water flow through a high aspect ratio rectangular microchannel was conducted to further understand fluid dynamic characteristics in microchannels and to test the validity of macroscale theories that are commonly utilized at the microscale. A rectangular microchannel with nominal dimensions of 500  $\mu\text{m}$  in height, 6 mm in width, and 32.8 cm in length was CNC machined into an aluminum blank. The test-section was completed by attaching a cap blank to the microchannel blank. Pressure and velocity data were obtained over a Reynolds number range from 173 to 4830, where the Reynolds number is based upon hydraulic diameter and channel average velocity. Velocity data were obtained using molecular tagging velocimetry (MTV). Laminar dimensionless velocity and coefficient of friction data are in agreement with macroscale theory. Transition from laminar flow, based upon a change in dimensionless velocity profile shape, occurs at a Reynolds number of 2800. This transitional Reynolds number is in excellent agreement with integral results and macroscale experimental results. Fully developed turbulent flow is found to exist at a Reynolds number of 4800. Inner normalized mean velocity profiles scale in the near-wall region, whereas the profiles of Reynolds stress and production of kinetic energy do not scale on inner variables. The inner normalized mean velocity profiles exhibit increasingly logarithmic-like behavior through the transitional regime. The experimental trends for the inner normalized mean velocity, Reynolds stress, and turbulence production are consistent with macroscale experimental and direct numerical simulation data. At this scale, influences reliably attributable to microscale effects were not detected in either the laminar or turbulent measurements of the present study.

© 2010 Elsevier Inc. All rights reserved.

### 1. Introduction

With advances in micro-fabrication technology, researchers are finding new uses for microfluidic devices for manipulating fluids in numerous scientific and industrial contexts [1]. For example, fluid transport is required in drug delivery and in chemical and DNA analysis in biomedical applications [2]. High Reynolds number applications are also being realized since micro-electro-mechanical-systems (MEMS) can be used in turbulent flows for improved flow diagnosis and control [3]. Additionally, Lempert et al. [4] investigated supersonic flow in microjets that could be employed for flow control and/or small satellite orbit maintenance. In order to optimize the design of microsystems, there is a need for an increased understanding of momentum transport in microchannels in the transitional and turbulent microflows.

The importance of understanding transitional and turbulent flows has substantial implications for heat transfer studies. As

originally discussed by Tuckerman and Pease [5], advantageous scaling effects at the microscale, e.g., increased surface area to volume ratio increases surface phenomena such as heat and mass transfer, enable enhanced heat transfer for very-large-scale-integrated circuits. Although a majority of microfluidic devices operate in the laminar regime, eventually applications could require turbulent flows to effectively dissipate heat and passively mix fluids. Designers cannot, however, reliably optimize microfluidic devices that operate in the transitional/turbulent regimes if macroscale correlations are not valid at the microscale. Velocimetry techniques, e.g., particle imaging velocimetry (PIV), are now being utilized to investigate transitional microscale flows. The first PIV study to encompass a large Reynolds number,  $Re_{D_h} = \rho V D_h / \mu$ , range in microchannels was performed by Sharp and Adrian [6] where  $\rho$  is the mass density,  $V$  is the spatial average velocity,  $D_h \equiv 4A/P$  is the hydraulic diameter,  $A$  is the cross-sectional area,  $P$  is the wetted perimeter, and  $\mu$  is the dynamic viscosity. Note that three Reynolds numbers are commonly referred to for channel flows and are utilized here. The first is  $Re_{D_h}$ , the second is based on the wall-to-wall average velocity,  $V_z$ , and wall-to-wall spacing,  $H$ , and is defined as  $Re_m = \rho V_z H / \mu$ , and the last is based on the friction velocity,  $u_\tau$ , and

\* Corresponding author. Tel.: +1 801 585 9730; fax: +1 801 585 9826.

E-mail address: [ameel@mech.utah.edu](mailto:ameel@mech.utah.edu) (T.A. Ameel).

## Nomenclature

$A$	cross-sectional area ( $\text{m}^2$ )	<i>Subscript</i>	
$B$	separation constant	<i>cl</i>	centerline
$C$	calibration constant (m/pixel)	<i>cr</i>	critical
$C_f$	coefficient of friction	<i>INT</i>	integral
$D_h$	hydraulic diameter ( $4A/P$ )	<i>LW</i>	left wall
$f$	friction factor	<i>max</i>	maximum
$H$	channel height (m)	<i>RW</i>	right wall
$L$	channel length (m)	<i>thry</i>	theory
$L_{t,i}$	pressure tap location (m)	<i>T</i>	total
$P$	wetted perimeter (m)		
$P^+$	inner normalized production of mean TKE	<i>Superscript</i>	
$r$	radial coordinate (m)	$+$	normalized by wall variables
$R$	radius (m)		
$R_i$	result of interest	<i>Greek symbols</i>	
$Re_{D_h}$	Reynolds number ( $\rho D_h V / \mu$ )	$\alpha$	aspect ratio ( $W/H$ )
$Re_m$	Reynolds number ( $V_z H_T / \nu$ )	$\delta$	channel half-height (m)
$Re_\tau$	Reynolds number ( $\delta u_\tau / \nu$ )	$\delta^+$	ratio of the outer-to-inner length scales ( $\delta u_\tau / \nu$ )
$t_0$	initial time (s)	$\delta R_i$	uncertainty for result of interest
$u_\tau$	friction velocity (m/s)	$\Delta P$	pressure drop (Pa)
$-\overline{u}v^+$	inner normalized Reynolds stress	$\Delta t$	delayed time (s)
$u_i$	instantaneous velocity (m/s)	$\Delta x$	streamwise displacement (pixel)
$U$	mean velocity (m/s)	$\epsilon_{rms}$	r.m.s. roughness ( $\mu\text{m}$ )
$U^+$	inner normalized mean velocity	$\epsilon_{rms}^+$	inner normalized r.m.s. roughness
$V$	spatial average velocity (m/s)	$\gamma$	offset (pixel)
$V_z$	wall-to-wall average velocity (m/s)	$\kappa$	von Karman constant
$W$	channel width (m)	$\eta$	outer normalized wall-normal position ( $y/\delta$ )
$x$	streamwise position (m)	$\nu$	kinematic viscosity ( $\text{m}^2/\text{s}$ )
$y$	wall-normal position (m)	$\rho$	mass density ( $\text{kg}/\text{m}^3$ )
$y_p$	wall-normal position (pixel)	$\sigma$	standard deviation
$y^+$	inner normalized wall-normal position ( $yu_\tau/\nu$ )	$\sigma_{95}$	95% confidence interval
$y_m^+$	peak location of $-\overline{u}v^+$	$\tau_w$	wall shear stress (Pa)
$y_p^+$	peak location of $P^+$	$\mu$	dynamic viscosity (Pa s)
$z$	spanwise position (m)		

the half channel spacing,  $\delta$ ,  $Re_\tau = \rho u_\tau \delta / \mu$ . They utilized microtubes over a Reynolds number range  $20 \leq Re_{D_h} \leq 2900$ . Transition was found to be around  $Re_{D_h} \approx 1800 - 2300$ . Only centerline PIV results were presented since the near-wall resolution was poor. The authors concluded that the behaviors of pressure drop, mean velocity, and r.m.s. velocity were consistent with macroscale theory.

Li et al. [7] also conducted experiments using PIV to investigate flow in a microchannel over the range  $272 \leq Re_{D_h} \leq 2853$ . The authors indicated that transition occurred at  $Re_{D_h} = 1535$  based upon a sudden increase in streamwise velocity fluctuations that continued to increase with increasing  $Re_{D_h}$ . Fully turbulent flow was evident at  $Re_{D_h}$  from 2630 to 2853 based upon a merging of the dimensionless velocity profiles. Li and Olsen [8] extended their earlier study to a  $Re_{D_h}$  range from 200 to 3971. The authors concluded that there was no evidence of early transition, with transition occurring in the range  $1718 \leq Re_{D_h} \leq 1885$ . Fully turbulent flow was found to exist over  $Re_{D_h}$  from 2600 to 2900. Li and Olsen [9], in a complimentary study, also determined the effect of channel aspect ratio on transitional and turbulent flows over the range  $200 \leq Re_{D_h} \leq 3267$ . Again, transition was reported to occur in the range  $1765 \leq Re_{D_h} \leq 2315$  with fully turbulent flow occurring in the range  $2600 \leq Re_{D_h} \leq 3200$ . For the aforementioned Li studies, velocity data were not presented for 5–20% of the channel cross-section due to decreasing near-wall resolution with increasing  $Re_{D_h}$ . Li and Olsen [10] determined that large-scale turbulent structures in microchannels exhibited similar characteristics to large-scale structures in macroscale pipes and ducts.

More recently, Natrajan and Christensen [11] investigated transitional capillary flow using PIV over the range  $1800 \leq Re_{D_h} \leq$

3400. Pressure drop measurements and velocity profiles indicated that transition occurred at  $Re_{D_h} \approx 1900$ . Fully developed turbulent flow was reported to exist at  $Re_{D_h} \approx 3400$ , based upon the agreement of the experimental mean velocity profile with a direct numerical simulation (DNS) mean velocity profile at  $Re_{D_h} = 5300$ . The authors also presented Reynolds stress profiles in the transitional and turbulent regimes. The Reynolds stress profiles exhibited similar trends to macroscale turbulent flows. In a companion study, Natrajan et al. [12] compared statistical and structural similarities between micro- and macroscale flows at  $Re_{D_h} = 4500$ . For the first time using a microtube, inner wall scalings were investigated at the microscale using the estimated streamwise pressure gradient to determine the friction velocity. The inner normalized mean velocity for  $r^+ = ru_\tau/\nu > 30$  was in agreement with those obtained from a DNS study where  $r$  was the radial coordinate. The superscript  $+$  indicates a dimensionless quantity scaled by the wall variables, i.e.,  $r^+ = ru_\tau/\nu$ , where  $\nu = \mu/\rho$  is the kinematic viscosity and  $u_\tau = (\tau_w/\rho)^{1/2}$  is the wall shear velocity. The Reynolds stress profile was qualitatively in agreement with the DNS data. The authors attributed the discrepancy in magnitude to a low fluctuating wall-normal velocity. The authors also noted that microscale turbulent flows, both structurally and statistically, appeared to be consistent with macroscale turbulent flows. For both studies, near-wall resolution was not possible for  $r/R < 0.1$  ( $r/R = 1$  was the centerline and  $R$  was the tube radius), due to wall curvature of the microtube.

Molecular tagging velocimetry (MTV) has also been used to investigate microscale laminar flows. MTV is a noninvasive laser based technique that can be thought of as the molecular counter-

part to PIV [13]. Instead of tracking particles, molecules that phosphoresce are tracked. In addition, because particles are replaced by molecules dissolved in the flowing medium, difficulties relating to particles tracking the flow, density mismatch between the fluid and particles, and particle seeding density are all absent from MTV [14]. Since the MTV technique does not require particle seeding, its spatial resolution matches that of the imaging resolution of the system. Therefore, MTV is an attractive technique for experiments at the microscale [15]. An ultraviolet (UV) source is used to photo-tag the fluid molecules that are subsequently imaged at an initial time,  $t_0$ , and a delayed time,  $t_0 + \Delta t$ , within the lifetime of the tracer. As in PIV, two images are compared and the velocity field is determined from the Lagrangian displacement of molecules between the two images. For an excellent presentation on the history of the MTV technique and its various implementations, see Koochesfahani and Nocera [16].

The first  $\mu$ MTV study to encompass a large  $Re_{D_h}$  range was conducted by Maynes and Webb [17]. They investigated flow in a 705  $\mu\text{m}$  microtube over a range  $500 \leq Re_{D_h} \leq 2390$ . The authors considered two macroscale image analysis techniques applied to microscale flows, (1) a line center method [18] and (2) a correlation method [19]. They found that the correlation method produced velocity profiles that were less sensitive to the broader MTV lines found at the microscale. The velocity profiles were in agreement with the fully developed analytical solution for flow in a tube for  $Re_{D_h} < 2100$ . For  $Re_{D_h} > 2100$ , the velocity profiles started to deviate from laminar flow theory, with the profile flattening near the centerline. Thompson et al. [20] continued the work of Maynes and Webb [17] by downscaling to a 148  $\mu\text{m}$  tube and  $Re_{D_h} = 140$ . Thompson et al. [21] also examined the hydrodynamic entrance length in a 180  $\mu\text{m}$  tube in the range  $60 \leq Re_{D_h} \leq 340$ . The classical entrance length criteria, e.g.,  $x/D = 0.05Re_{D_h}$  was found to be an accurate representation for flows at the microscale, where  $x$  is the streamwise direction. Experimental velocity profiles in the fully developed region were in agreement with the laminar flow analytical solution for fully developed pipe flow. Lum [22] used  $\mu$ MTV to measure velocity profiles in a high aspect ratio duct for the range  $0.32 < Re_{D_h} < 138$ . High near-wall resolution was obtained so that a direct measurement of the wall shear stress could be determined. The wall shear stress was in agreement with those predicted using the analytical duct solution for rectangular channel flow.

The recent literature indicate that microscale laminar flows are in agreement with macroscale theory for liquids flowing in microscale ducts. Limited turbulent data for mean and instantaneous velocity profiles, r.m.s. velocity, and Reynolds stress profiles have been published. Moreover, only one researcher has presented near-wall results, e.g., wall shear stress, over limited  $Re_{D_h}$  [22]. Such data are essential to understand momentum transport at the microscale. Previous MTV data have been limited to low Reynolds numbers. This is further motivation for performing a thorough investigation of laminar, transitional, and turbulent flow in a carefully characterized high aspect ratio microchannel using the MTV technique, which is the objective of this research. Of particular interest are data leading to an understanding of fluid flow for transitional and turbulent microflows. Mean fully developed velocity profiles as a function of Reynolds number were obtained over  $180 < Re_{D_h} < 4830$ . High aspect ratio microchannels are relevant to microfluidic devices since they are much more easily fabricated than circular geometries. This is largely due to constraints imposed by current manufacturing techniques, e.g., photolithography and micromachining. An additional benefit is that optical issues due to tube wall curvature are alleviated. This study extends the earlier MTV study of Lum [22] by covering laminar, transitional, and turbulent channel flow, instead of only a portion of the laminar regime ( $0.32 < Re_{D_h} < 138$ ). A novel device designed

for the implementation of the MTV technique and simultaneous bulk flow data acquisition was manufactured to withstand the high pressure drop required for high  $Re_{D_h}$  studies. Transitional profiles provide a direct determination of the critical Reynolds number, which can be compared to the value obtained from integral friction data. Due to the high spatial resolution and ability to obtain near-wall data using MTV, this study allows for an investigation into the inner scaling of the mean velocity, Reynolds stress, and production of turbulent kinetic energy for transitional/turbulent microscale flows. The high spatial resolution is advantageous in comparison to transitional PIV studies since the resolution is sufficient to resolve important near-wall features such as the peak in Reynolds stress.

## 2. Methods and procedures

### 2.1. Test section design, manufacturing, and assembly

A rectangular microchannel designed with dimensions 500  $\mu\text{m} \times 6 \text{ mm} \times 32.77 \text{ cm}$  ( $H \times W \times L$ ) was used for the microchannel experiments, where  $W$  is the width and  $L$  is the length. For turbulent flows, Dean [23] analyzed a large set of available data and found that three-dimensional effects slightly disturb the flow near the centerline if the aspect ratio,  $\alpha = W/H < 7$ . An aspect ratio of 12 is thought to produce a nearly 2D channel flow and such a channel has been used for macroscale turbulent studies [24].

The entrance length for laminar flows is nominally  $x/D_h = 0.08Re_{D_h}$  [25]. Also, transition occurs at  $Re_{D_h} \approx 2300$  [26]. Using the aforementioned results, the entrance length is designed for  $184D_h$ . According to Lien et al. [27], one can expect fully turbulent flow for development lengths exceeding about 150 channel heights. Thus, the entrance length for this study,  $184D_h$ , ensures that the flow reaches a fully developed state in the streamwise direction for all  $Re_{D_h}$  investigated.

Pressure taps, 250  $\mu\text{m}$  in diameter, located at  $x/D_h = 185.9$  and 349.6 were employed to measure the pressure drop in the fully developed zone, see Fig. 1. The upstream pressure port is located at a point where fully developed flow is established for all  $Re_{D_h}$ , eliminating the need to take into account entrance pressure loss. The downstream tap is located at  $x/D_h = 5.41$  from the microchannel exit so that exit losses do not have to be taken into account. The wall temperature was measured using T-type thermocouples, with an unshielded junction located at the same streamwise locations as the pressure taps. The fluid temperature may be assumed to be equivalent to the wall temperature due to the high thermal conductivity of the test-section material, aluminum 6061-T6, and the thin separation distance between the thermocouple and fluid ( $\approx 250 \mu\text{m}$ ).

Optical access was required for the laser beam to enter/exit the microchannel and to allow the phosphorescent emission to be captured by the ICCD camera. Two UV fused silica cylindrical windows were used to allow the UV laser light to enter/exit the microchannel. The windows were centered at a streamwise location of  $x/$

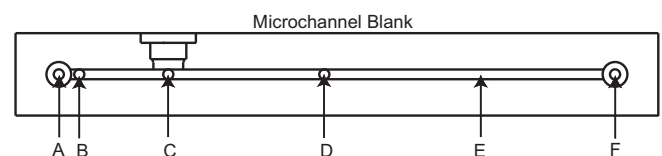


**Fig. 1.** Essential design features of the test-section design. Description: A – outlet port, B – downstream pressure (microchannel blank) and temperature measurement (cap blank, not shown), C – MTV and imaging access, D – upstream pressure (microchannel blank) and temperature measurement (cap blank, not shown), E – microchannel, and F – inlet port.

$D_h = 290.1$ . A UV grade fused silica window allowed the phosphorescent light to pass from the microchannel to an ICCD camera objective. This window was centered above the laser access windows and is perpendicular to the flow direction, see Fig. 1. The test-section was formed from two identical 6061 T-6 aluminum blanks, one of which was CNC machined to form the microchannel and the other the cap. The blanks have dimensions of  $50.8 \times 20.0 \times 396.2$  mm.

## 2.2. Characterization

### 2.2.1. Height and width

To obtain height and width measurements of the microchannel, the microchannel was sectioned using a wire-EDM into five sections. This sectioning allowed 10 measurements of the microchannel height and width. A scanning electron microscope (SEM) was used to obtain the height measurement. Since the channel was too wide to be imaged in its entirety, SEM images were taken at the bottom, middle, and top of the microchannel at each cross-section. An SEM image of the top of the microchannel is shown in Fig. 2. An SEM standard was used as a reference length and has an antireflective chromium grid pattern printed on a quartz substrate with an uncertainty of  $\pm 0.1 \mu\text{m pitch}^{-1}$  for the  $50 \mu\text{m}$  pitch pattern. Both the microchannel and standard were imaged at the same magnification and working distance. Sixteen measurements at each streamwise location were made at the bottom, middle, and top of the channel; these 48 measurements were then averaged. The average channel height was  $509.1 \mu\text{m}$  with an uncertainty of  $\pm 4.14 \mu\text{m}$ . The data indicate the channel height was uniform along the length and width of the channel except for a slight increase of about  $3.1 \mu\text{m}$  near the laser access windows.

The channel width was measured using a profile projector equipped with a  $50\times$  objective with a stage resolution of  $1 \mu\text{m}$ . Thirty measurements were taken at the streamwise locations where the height measurements were acquired. The results were then averaged at each location to determine the width. The channel width was  $5.99 \text{ mm}$  with an uncertainty of  $\pm 10.1 \mu\text{m}$  and the results indicate that the channel width was uniform within  $0.08\%$  along the length of the channel.

### 2.2.2. Surface roughness and optical access window offset

Optical profilometry was used to determine surface roughness. Roughness measurements were obtained on both blanks between each streamwise location at which height and width measurements were made. Two scans were made over an area of

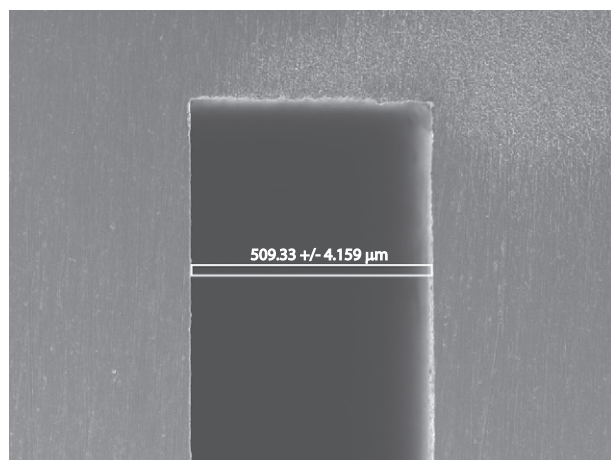


Fig. 2.  $100\times$  SEM image of the top of the channel. Also shown is the thin rectangle used to determine microchannel height.

$3.59 \text{ mm}$  in the streamwise direction and  $2.70 \text{ mm}$  in the spanwise direction and then averaged. The roughness data were not filtered and roughness measurements were not made for the small side-walls. Averaging over all of the scans, the r.m.s. roughness,  $\epsilon_{rms}$ , for the left wall was  $0.717 \mu\text{m}$  and  $0.434 \mu\text{m}$  for the right wall. The relative roughness for the channel,  $\epsilon_{rms}/D_h = 0.000613$ , where  $\epsilon_{rms}$  is obtained by averaging the left and right wall  $\epsilon_{rms}$  values.

The flushness of the optical windows used to pass the UV laser light was verified using a stylus-based profilometer. Profilometer scans were made along the centerline of the channel in both the streamwise and spanwise directions. From these scans, the offset distance from the blanks to the center of the fused silica windows were determined (where MTV data were acquired). The average offset value was  $5.8 \mu\text{m}$  for the left wall (laser beam ingress) and  $7.1 \mu\text{m}$  for the right wall (laser beam egress). The total offset (towards the channel center), accounting for both the top and bottom windows, was  $2.5\%$  of the wall-to-wall spacing. Further, the MTV interrogation location was  $413$  offset heights downstream from the step. At this streamwise distance, the influence of the step change on the local dynamics is expected to be negligible. However, due to the offset of the optical access windows,  $1\text{--}2$  near-wall data points, approximately  $3\text{--}6 \mu\text{m}$ , could not be imaged. Table 1 presents the results of the characterization analysis. The total uncertainty with  $95\%$  confidence in the geometric parameters presented in Table 1 was comprised of the systematic and random measurement errors [28].

## 2.3. Experimental apparatus

### 2.3.1. MTV

A Princeton 8-bit video ICCD camera was used to acquire the MTV time-delayed and initial images at a rate of  $60 \text{ Hz}$ . A  $10\times$  infinity corrected Mitutoyo objective was used along with a C-mount extension tube. The objective has a field of view of  $0.66 \times 0.88 \text{ mm}$  and an numerical aperture of  $0.28$ . The out-of-plane resolution was set by the camera objective's depth of focus, which for this lens is  $3.5 \mu\text{m}$ . A pulse generator was used to trigger the ICCD in response to the laser firing as well as control the camera exposure time and delay. The time delay after laser firing and initial image capture, time delay between image capture, and camera exposure time were measured using an oscilloscope.

An excimer laser filled with XeCl gas provided the UV source. The  $308 \text{ nm}$  beam exiting the laser has an energy density of  $55 \text{ mJ cm}^{-2}$ , an energy output of  $110 \text{ mJ}$ , and a pulse width of  $9 \text{ ns}$ . Standard UV fused silica optics were employed and the resulting beam waist was nominally  $75 \mu\text{m}$ . To obtain this beam size, the beam exiting the laser cavity was passed through a  $1 \text{ mm}$  circular pinhole filter. The resulting  $1 \text{ mm}$  beam then passed through a  $200 \text{ mm}$  spatial filter utilizing a  $150 \mu\text{m}$  pinhole. The beam was then recollimated using a  $100 \text{ mm}$  focal length plano-convex lens. A  $100 \text{ mm}$  meniscus lens and  $12.5 \text{ mm}$  plano-convex lens combination were employed after the spatial filter to focus the beam to  $75 \mu\text{m}$  FWHM (full width – at half maximum). The full width at half maximum (FWHM) method outlined by Lum [22] was employed to determine the beam width. In this method the reported beam width corresponds to the distance between points of phosphorescence intensity at intensity values one half of the maximum intensity, which nominally corresponds to the center of the intensity distribution. The energy density at the microchannel was estimated to be less than  $2 \text{ J cm}^{-2}$ , which accounts for losses in the optics and energy reduction at both pinholes.

### 2.3.2. MTV solution

This implementation of the MTV technique used the ternary molecular complex developed by Ponce et al. [29] consisting of  $1 - Br Np \cdot G\beta - CD \cdot ROH$ , where  $1 - Br Np$  is bromonaphthalene,



**Table 1**

Summary of the characterization results, where  $L_{t,i}$  is the pressure tap location,  $\sigma$  is the standard deviation, and  $\sigma_{95}$  is the 95% confidence interval,  $R_i$  is the result of interest and  $\delta R_i$  is the associated uncertainty.

Feature	Symbol	$R_i$ ( $\mu\text{m}$ )	$\sigma$ ( $\mu\text{m}$ )	$\sigma_{95}$ ( $\mu\text{m}$ )	$\delta R_i$ ( $\mu\text{m}$ )	$(\delta R_i/R_i)$ (%)
Channel height	$H$	509.1	2.56	0.233	4.15	0.82
Channel width	$W$	5990.2	6.76	0.078	10.1	0.17
Channel height MTV	$H_{MTV}$	512.2	1.44	0.294	4.15	0.81
Offset left wall	$\gamma_{LW}$	5.84	1.78	0.147	0.147	2.52
Offset right wall	$\gamma_{RW}$	7.06	2.36	0.195	0.195	2.76
Pressure tap	$L_{t,1}$	205,890	NA	NA	25.0	0.01
Pressure tap	$L_{t,2}$	356,950	NA	NA	25.0	0.01
r.m.s. roughness	$\epsilon_{rms}$	0.575	0.154	0.064	0.064	11.2

$G\beta$  – CD is a cyclodextrin, and ROH is an alcohol. Cyclohexanol was used as the ROH with a molar concentration of 0.1 M. Following the suggestion of previous researchers, the concentration of the  $G\beta$  – CD was  $2 \times 10^{-4}$  M and the concentration of bromonaphthalene was always kept in excess to maintain a saturated solution, typically a molar concentration of  $1 \times 10^{-5}$  M [29,30]. For more information regarding the MTV solution chemistry, see Koochesfahani and Nocera [16].

### 2.3.3. Bulk flow measurements

A schematic of the experimental setup is shown in Fig. 3. The flow facility has been described elsewhere by Costaschuk et al. [26]. A National Instruments PXI-1010 data acquisition system was used to acquire and record all mass measurements, pressures, time, and temperatures. For laminar and transitional flows, a differential pressure transducer with a range of 0 to 34.47 kPa (5 psid) and uncertainty of 0.25% of full scale was used to measure the in-channel pressure drop. For turbulent flows, a 1.38 MPa (300 psig) sensor was utilized for the upstream pressure measurement and a 2.07 MPa (200 psig) sensor for the downstream measurement. The uncertainty of both sensors is 0.15% of full scale. T-type thermocouples used to measure the wall temperature were

500.8  $\mu\text{m}$  in diameter with an uncertainty of  $\pm 1.0^\circ\text{C}$ . The uncertainties in the mass and time measurements are  $\pm 0.01$  gm and  $\pm 0.01$  s, respectively.

## 2.4. Data acquisition

### 2.4.1. MTV image acquisition

For laminar, transitional, and turbulent flows, the camera exposure time ranges were 10–40  $\mu\text{s}$ , 10–15  $\mu\text{s}$ , 7.2–10  $\mu\text{s}$ , respectively, and time delay ranges were 30–600  $\mu\text{s}$ , 30  $\mu\text{s}$ , and 25  $\mu\text{s}$ , respectively. For laminar flows, initial images were acquired  $t_0 = 15.8$   $\mu\text{s}$  after the laser fires and for transitional/turbulent flows,  $t_0 = 6$   $\mu\text{s}$ . The uncertainty in determining the time delay, which was based upon the manufacture's specifications for the oscilloscope, was:  $\pm 2$   $\mu\text{s}$  for  $150 < \Delta t < 600$   $\mu\text{s}$ ,  $\pm 0.5$   $\mu\text{s}$  for  $80 < \Delta t < 150$   $\mu\text{s}$ , and  $\pm 0.1$   $\mu\text{s}$  for  $5 < \Delta t < 80$   $\mu\text{s}$ . The camera exposure time was set to the same value for the acquisition of both initial and time-delayed images. All exposure and delay times for all flow rates were optimized to obtain the highest possible signal-to-noise ratio.

In a single experiment, 190 instantaneous images were captured. This was the maximum number of images that the frame-grabber could capture before writing to disk. The resulting 190 instantaneous images were averaged to create a single mean image. This image capture and averaging process was repeated until the running average converged within 1.0%. Image averaging was implemented since the instantaneous images exhibited unacceptably high signal noise. The lower than desired signal-to-noise can be attributed to the low quantum efficiency of the MTV tracer, approximately 3.5%, in comparison to uncaged fluorescein, which has a quantum efficiency of 90% [30]. Also, the amount of photons collected by the ICCD is proportional to the volume of fluid illuminated [21].

### 2.4.2. Bulk flow data acquisition

All mass, pressure, time, and temperature data were acquired after the system attained a steady state. Bulk flow data were obtained simultaneously with the time-delayed and initial MTV image acquisition for  $Re_{D_h} < 3000$ . For  $Re_{D_h} > 3000$ , three sets of bulk flow data were acquired. Bulk flow data were acquired before and after the time-delayed MTV images were acquired and then after initial MTV image acquisition. This change in data acquisition method at high  $Re_{D_h}$  was required due to the high mass flow rate and limited capacity of the mass balance. The flow steadiness of the system was verified from the pressure drop standard deviation and changes in mass flow rate with time. Constant mass flow rate was essential since the final images, both time-delayed and initial, were ensemble averaged and not acquired simultaneously. Typically, the pressure drop standard deviation normalized by the mean value of the measured pressure drop during image acquisition was less than 0.01, which indicated that the flow was steady over acquisition of the initial and time-delayed images. Further, the r.m.s.  $Re_{D_h}$  normalized by the average  $Re_{D_h}$  during the time-delayed and initial image acquisition was less than 0.01, which indicated that the overall experimental conditions were nearly identical during the time-delayed and initial image acquisition.

## 2.5. Data reduction

### 2.5.1. MTV image reduction

The streamwise displacement,  $\Delta x$ , at each wall-normal pixel location,  $y_p$ , was determined by correlating the initial image intensity distribution with the time-delayed image. The  $\mu\text{MTV}$  correlation method has been described elsewhere [17,20,21]. Using the correlation method, the maximum average displacement for all laminar and turbulent flows was 52 pixels and 38 pixels, respectively. Uncertainty in the displacement for laminar flows with

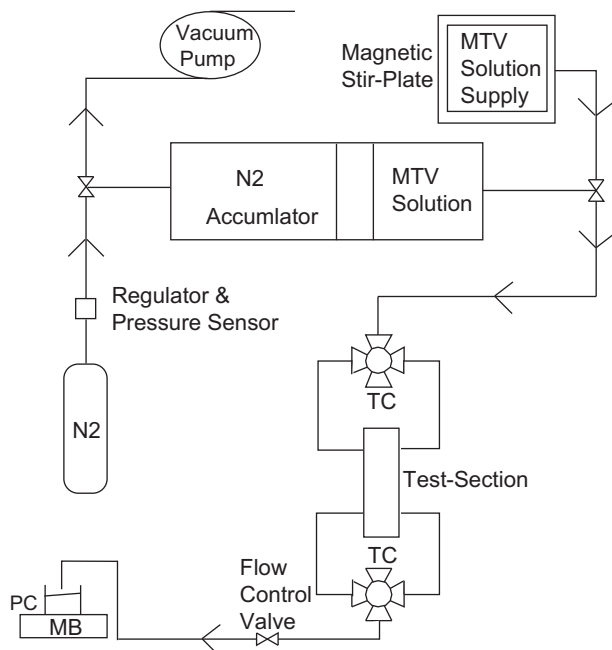


**Fig. 3.** Schematic of the experimental apparatus. Description: MB – mass balance; PC – plastic container; and TC – T-type thermocouple.

95% confidence was  $\pm 0.01 \Delta x_{\max}$ , where  $\Delta x_{\max}$  is the maximum displacement in pixels [21] and for transitional/turbulent flows, the uncertainty was estimated to be  $\pm 1.0$  pixel. A typical correlation window is shown in Fig. 4, along with a superposition of the initial and time-delayed line images for laminar flow.

The mean displacement profiles were obtained by averaging 900 frames for laminar flows and 1900 images for transitional/turbulent flows. Least-squares smoothing developed by Savitzky and Golay [31] was employed to smooth the mean displacement profiles. The effect was modest, with greater than 95% of the data being modified less than the uncertainty of the experiment. This approach was also used in macroscale MTV studies by Hill and Klewicki [18] and Thurlow and Klewicki [32].

Once the displacement across the channel height was determined and smoothed, the wall locations were determined. Due to the no-slip boundary condition, the displacement at the wall is zero. To locate the walls with subpixel accuracy for laminar flows, a parabolic curve-fit to the entire displacement profile was used. The roots of the resulting polynomial were then determined, providing the fluid wall locations. For turbulent flows, the wall locations were estimated using a linear curve-fit to the first/last six displacement data points and finding the root of the resulting linear expression. The downside to this approach is that there are two unknown coefficients in the linear fit, i.e., the intercept and the slope. To find the actual wall location, the offset in wall location was determined by averaging the offset required for the estimated  $y$ -location to coincide with the linear sublayer. Mathematically,

$$\begin{aligned} U^+ &= y^+ \\ \frac{U}{\sqrt{\tau_w/\rho}} &= \frac{y\sqrt{\tau_w/\rho}}{v} \\ \frac{C\Delta x}{\Delta t} &= (y_p + \gamma)C \frac{\tau_w/\rho}{v} \\ \Delta x &= (y_p + \gamma) \frac{\tau_w/\rho}{v} \end{aligned} \quad (1)$$

where,  $y$  is the dimensional wall-normal position,  $C$  is a constant,  $\tau_w$  is the wall shear stress obtained from the measured pressure drop and  $\gamma$  is the offset. Using the above method, the first three offset points were averaged to determine the wall location, with average offset being  $-0.767$  pixels. Increased accuracy in the wall location is obtained with this method since the calculation includes the best estimate for the wall shear stress – that determined from the independent pressure drop measurements and only using the data to

determine the intercept. Based upon the work by Thompson et al. [21], the uncertainty for the wall location was estimated to  $\pm 1.0$  pixel and the offset values for all data sets fall within this range.

In order to convert from pixel space to dimensional space, a calibration constant,  $C$ , was required. To determine  $C$ , the channel height was employed as a known physical dimension. For laminar flows, averaging over 27 flow scenarios, the calibration constant was determined to be,  $C = 3.04 \mu\text{m pixel}^{-1}$  with an uncertainty of  $7.39 \times 10^{-2} \mu\text{m pixel}^{-1}$ . For turbulent flows, averaging over 18 flow scenarios,  $C = 3.10 \mu\text{m pixel}^{-1}$  with an uncertainty of  $7.64 \times 10^{-2} \mu\text{m pixel}^{-1}$ . The uncertainty in the calibration constant was determined using the method outlined by Moffat [33] and comprised of uncertainty in both wall locations,  $\pm 1.0$  pixel, and total channel height,  $\delta H_T = 4.2 \mu\text{m}$ .

### 2.5.2. Wall gradient

For laminar flows, the velocity gradient at the wall was determined by curve-fitting a second-order polynomial to the entire velocity profile and computing the derivative at the wall. For turbulent flows, the first five velocity data points were curve-fit to a linear profile (for all flows, the first five data points correspond to  $y^+ < 5.2$ ). The uncertainty in wall gradient was based upon the standard error in the curve-fit coefficients. Using the matrix formulation method for least squares outlined by Chapra and Canale [34], the variance and covariance, and therefore, standard error for the curve-fit coefficients were determined. It is also possible to determine the 95% confidence interval on the standard error using the Student  $t$ -multiplier, which was based upon the number of data points used in the curve-fit and confidence interval [28]. Using the standard error and  $t$ -multiplier, the uncertainty with confidence in the wall gradient can be determined. For laminar flows, the wall gradient was obtained from a parabolic fit of the local smoothed velocity data. Therefore, only the variance for the linear coefficient was required since the constant and second-order coefficient are zero after differentiation and evaluation of the curve-fit polynomial at the wall. For turbulent flows, the gradient was obtained from a linear fit of the local smoothed velocity data; therefore, only the variance for the slope coefficient was needed.

### 2.5.3. Turbulent flow behaviors

The turbulent regime data were used for an investigation of whether the mean flow properties were consistent with those found at the macroscale. For this document, when discussing scaling of transitional and turbulent flows,  $u_i$  represents a fluctuating velocity,  $U_i$  represents the mean velocity, and  $\overline{(\cdot)}$  represents a time average. At the macroscale, the literature indicates that the logarithmic law is an accurate description for the mean velocity profile [24,35]. The inner normalized form of the logarithmic law, is given by

$$U^+ = \frac{1}{\kappa} \ln(y^+) + B, \quad (2)$$

where  $\kappa$  is the von Karman constant with typical value of 0.41 and  $B$  is an integration constant with a value of 5.0–5.5 [36].

The friction velocity,  $u_\tau$ , is often taken as the appropriate characteristic velocity, and thus its determination is essential for the purposes of scaling. For this work,  $u_\tau$  was determined from an integral momentum balance, and is given as

$$u_\tau = \sqrt{\frac{\delta \Delta P}{\rho L}}, \quad (3)$$

where  $\Delta P$  is the static pressure drop and  $L$  is the distance between pressure taps. It is of interest to estimate the Reynolds stress, and this was done using the once integrated momentum equation [37],

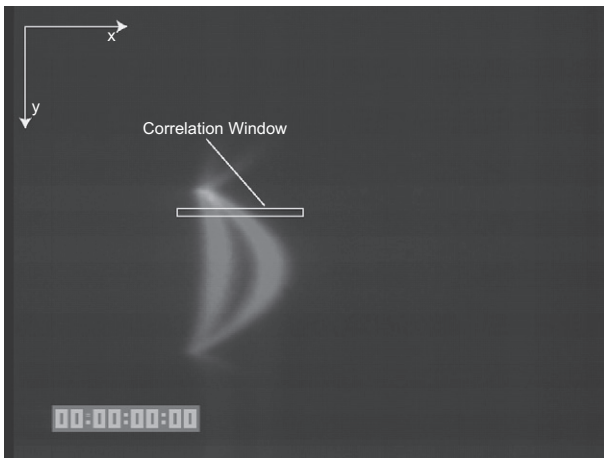


Fig. 4. Superposition of the initial and time-delayed images. A typical correlation window used in the data reduction method is also shown.

$$-\overline{uv} = -\nu \frac{dU}{dy} + u_\tau^2 \left(1 - \frac{y}{\delta}\right). \quad (4)$$

The viscous stress was calculated using a first order finite-difference scheme with  $O(h^4)$  accuracy, where  $h$  is the step size. If  $\delta^+ = \delta u_\tau / \nu$  is absorbed into the length scale for  $y$ , i.e., inner normalized, Eq. (4) is written as

$$-\overline{uv}^+ + \frac{dU^+}{dy^+} = 1 - \frac{y^+}{\delta^+}. \quad (5)$$

Further, if one scales  $-\overline{uv}$  by  $u_\tau$ , over the same region, and  $\delta^+$  is absorbed into the viscous stress, i.e., outer normalized, then Eq. (4) becomes

$$-\overline{uv}^+ + \frac{1}{\delta^+} \frac{dU^+}{d\eta} = 1 - \eta, \quad (6)$$

where  $\eta = y/\delta = y^+/\delta^+$ .

#### 2.5.4. Pressure drop data reduction

The Darcy–Weisbach equation, presented by Fox and McDonald [38] for an incompressible, fully developed flow, relates the Darcy friction factor,  $f$ , to pressure drop in the channel and is given as

$$f = \frac{2\Delta P D_h}{\rho L V^2}. \quad (7)$$

The spatial average of the velocity profile,  $V$ , was computed from the mass flow rate, as obtained from the measured mass measurements over a known time interval and  $L = L_{t,2} - L_{t,1}$ . The fluid density as a function of temperature is computed from a correlation presented by Hyland and Wexler [39]. The dynamic viscosity as a function of temperature is also computed from a correlation presented by Nagashima [40]. Both correlations use the average temperature determined from the wall temperature measurements. Viscosity and density of the MTV solution are approximately the same as for pure water, since the chemical concentrations are negligibly small [22]. Further experimental details may be found in Elsnab [41].

### 3. Results and discussion

#### 3.1. Pressure data

Using Eq. (7),  $f$  was determined for laminar, transitional, and turbulent flows. Experimental friction factor data along with the predicted  $f$  for laminar and turbulent flows are shown in Fig. 5. The agreement between the experimental and theoretical  $f$  data for laminar and turbulent flows is excellent. The uncertainty in  $f$

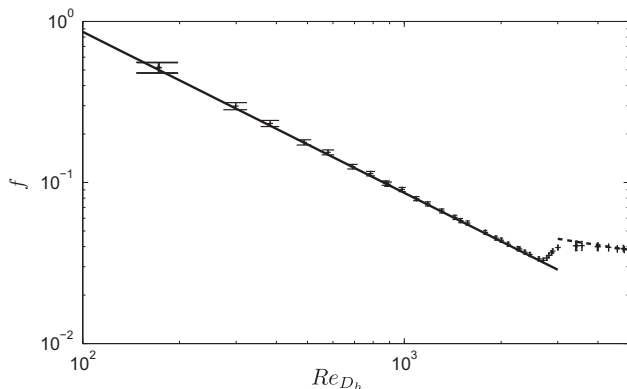


**Fig. 5.** Integral friction factors for all  $Re_{D_h}$  along with error bars for  $f$ . Description: +, integral data; solid line,  $f = 86.2/Re_{D_h}$  [25]; and dashed line,  $1/f^{1/2} = -1.8 \log[6.9/Re_{D_h} + (\epsilon_{rms}/D_h/3.7)^{1.11}]$  [42].

for laminar and transitional flows ranges from 2.89–7.34%, with the largest uncertainty associated with the smallest  $Re_{D_h}$  explored. For turbulent flows,  $Re_{D_h} > 3000$ , the uncertainty ranges from 4.48–6.87%, with the largest uncertainty again associated with the smallest  $Re_{D_h}$ . For both laminar and turbulent flows, the higher uncertainty is due to the small measured pressure relative to the maximum measurable pressure for the respective pressure sensor. The uncertainty in  $Re_{D_h}$  for all flows ranges from 0.85–1.31%. The Haaland equation [42], an explicit macroscale correlation for the turbulent friction factor, offers excellent agreement with the experimentally determined friction factors for  $3000 < Re_{D_h} < 4800$ . In addition, the critical Reynolds number,  $Re_{cr}$ , can be determined from an analysis of the friction factor data. The onset of transition is defined here when  $\log(f)$  deviates from its linear dependence on  $\log(Re_{D_h})$  for increasing  $Re_{D_h}$ .  $Re_{cr}$  is graphically determined from Fig. 5 and when defined this way,  $Re_{cr} = 2750$ . The  $f$  trends depicted are similar to the recent results presented in the literature [6,26,43].

#### 3.2. MTV data

##### 3.2.1. Laminar flow

Velocity profiles nondimensionalized with the average velocity obtained from the MTV data are shown in Fig. 6 over  $173 \leq Re_{D_h} \leq 2619$ . The wall-to-wall average velocity at a specific spanwise location,  $V_z$ , is obtained by numerically integrating the experimental velocity profile using the trapezoidal rule. Nondimensional velocity profiles are in excellent agreement with macroscale theory. For this high aspect ratio channel, at the microchannel centerline in the spanwise direction, the analytical duct solution is identical to the parallel plates solution [25]. Near-wall data range from  $y/H \lesssim 0.05$  for the cap blank wall and  $y/H \gtrsim 0.95$  for the microchannel blank wall, where  $0 \leq y \leq 525.2 \mu\text{m}$ . For this work, near-wall data refers to the first/last near-wall location where experimental velocities are obtained. The near-wall resolution was primarily dependent upon the image quality near the wall. Typically, the uncertainty for the centerline velocity measurement is 3%. The uncertainty in spatial location ranges from approximately 0 to 2.5%. With reference to Fig. 6, it is interesting to note that the measurement uncertainty associated with the deviation in the dimensionless velocity data compared to the analytical solution is a measure of the absolute uncertainty.

Theoretically, the ratio of the centerline velocity,  $u_{cl}$ , to the average velocity is constant for laminar flows. The theoretical ratio of the centerline velocity to the wall-to-wall average velocity at the channel midplane is  $u_{cl}/V_z = 1.5$ . This is in comparison to the ratio

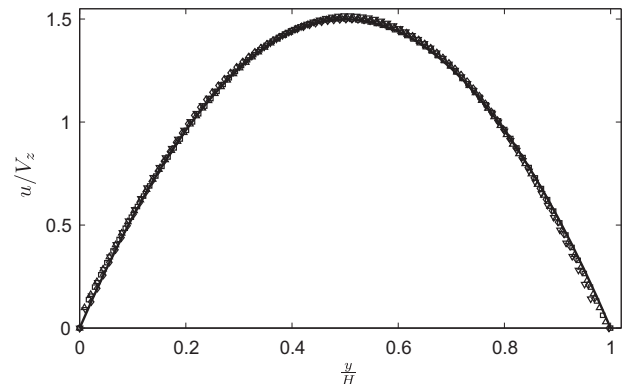


**Fig. 6.** Nondimensional experimental and analytical laminar velocity profiles for  $173 \leq Re_{D_h} \leq 2619$ . Note: Every third data point is shown. Description:  $\diamond$ ,  $Re_{D_h} = 173$ ;  $\square$ ,  $Re_{D_h} = 1090$ ;  $\triangle$ ,  $Re_{D_h} = 1925$ ;  $\nabla$ ,  $Re_{D_h} = 2619$ ; and solid line, laminar theory [25].

of the centerline velocity to the average duct velocity ratio of  $u_{cl}/V = 1.588$ . The theoretical  $V_z$  was obtained by integrating the velocity profile for the analytical duct solution in the wall-normal direction and evaluating the resulting expression at the microchannel centerline in the spanwise direction [25]. The experimental data are in excellent agreement with fully developed laminar flow theory as shown in Fig. 7 where  $u_{cl}/V_z$  is shown as a function of  $Re_m$ , where  $Re_m = V_z H_T/\nu$  and  $H_T$  is the total channel height where the MTV data are obtained, i.e., sum of the optical window offsets and  $H_{MTV}$ . Averaging over all  $Re_m$ ,  $u_{cl}/V_z = 1.507 \pm 8.85 \times 10^{-3}$ . Error bars are also shown in Fig. 7, with uncertainty in  $u_{cl}/V_z$  measurement ranging from 3.7–4.45%.

The dimensionless shear stress,  $C_f = \tau_w/(1/2\rho V_z^2)$ , is obtained from the wall-normal gradient of the velocity profile, experimental average velocity, and transport properties. Theoretically, the product of  $C_f Re_m$  is also a constant for laminar flows. For this geometry at the transverse midplane of the channel, the theoretical coefficient of friction is  $C_{f,thy} = 12/Re_m$ . The normalized coefficient of friction,  $C_f^* = C_f/C_{f,thy}$ , data along with error bars are presented in Fig. 8 as a function of  $Re_m$  with an uncertainty ranging from 5.2–7.5%. The data are in agreement with macroscale theory within the uncertainty of the experiment. Lum [22], using  $\mu$ MTV, also found that  $C_f^*$  was in agreement with macroscale theory for a high aspect ratio duct flow.

### 3.3. Transitional and turbulent flow

As  $Re_{D_h}$  increases, the flow eventually transitions from a laminar to a turbulent state. When transition occurs, the shape of the

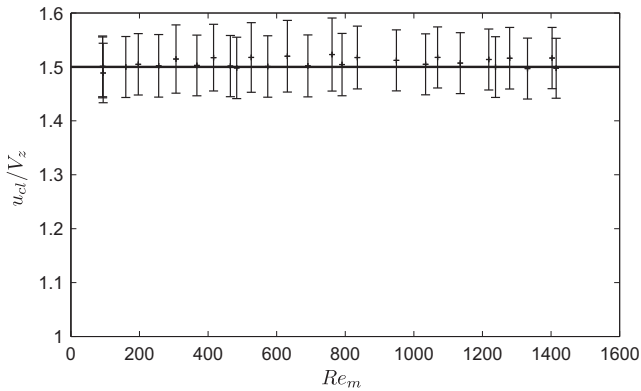


**Fig. 7.** Ratio of the centerline velocity to the average velocity for laminar flows along with the associated error bars. Description: solid line, laminar theory [25] and +, experimental data.

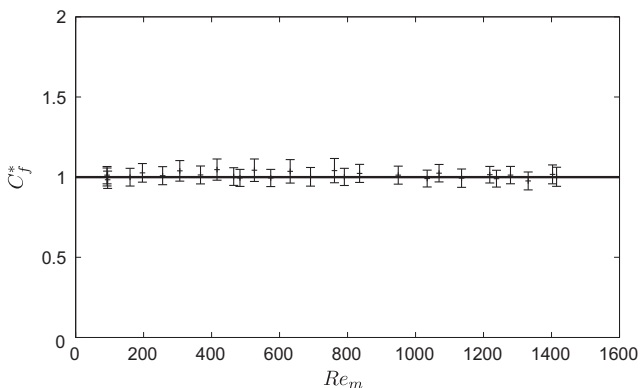


**Fig. 8.** Normalized coefficient of friction for laminar flows. Description: +,  $C_f^*$  and solid line, laminar theory.

dimensionless velocity profile changes. For laminar flows the velocity profile is parabolic. For turbulent and transitional flows the velocity profile flattens in the center of the channel and increases in the near-wall region [44]. When the time mean profile is normalized by the average velocity,  $u/V$ , and plotted versus  $y/H$ , the area under the curve is constant and equal to one. Therefore, the area lost in the center region is gained in the near-wall region. This trend is clearly evident for the dimensionless velocity profiles presented in Fig. 9. At  $Re_{D_h} = 2772$ , the velocity profile still depicts a parabolic shape, but at  $Re_{D_h} = 2817$ , the dimensionless centerline velocity slightly decreases and the velocity in the near-wall regions slightly increases. Based upon a change in dimensionless velocity profile shape,  $Re_{cr}$  is approximately 2800. For the present experiments,  $Re_{cr}$  is found from the pressure drop data to be approximately 2750. Patel and Head [45], in a macroscale study, reported that transition occurred at  $Re_m = 1350$ , for a high aspect ratio channel ( $\alpha = 48$ ) and for this study, transition occurred at  $Re_m \approx 1400$ . The onset of transition in microchannel flows has recently been reported to occur in the range  $1535 < Re_{cr} < 2374$ , which is lower than  $Re_{cr}$  for this microchannel ( $Re_{cr} \approx 2800$ ) [7–9,26].

As  $Re_{D_h}$  continues to increase, the centerline velocity continues to decrease while the velocity in the near-wall region increases. The rate at which  $u_{cl}/V_z$  decreases with increasing  $Re$  is shown in Figs. 9 and 10. Dean's correlation [23] is also shown in Fig. 10,  $u_{cl}/V_z = 1.28Re_m^{-0.0116}$ , which is only valid over  $6.0 \times 10^3 < Re_m <$

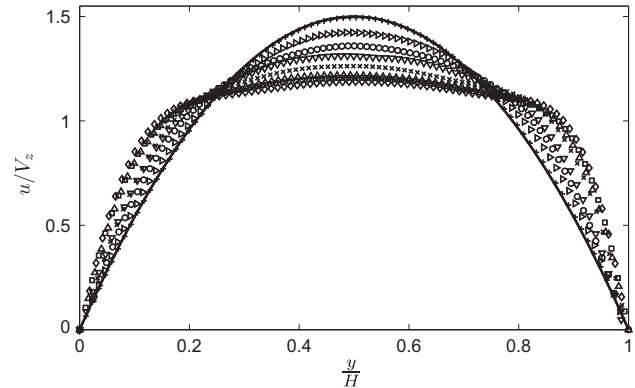


**Fig. 9.** Dimensionless transitional velocity profiles. Note: Every third data point is shown. Description: +,  $Re_{D_h} = 2772$ ;  $\nabla$ ,  $Re_{D_h} = 2817$ ;  $\circ$ ,  $Re_{D_h} = 2893$ ;  $\nabla$ ,  $Re_{D_h} = 3012$ ;  $\times$ ,  $Re_{D_h} = 3568$ ;  $\triangle$ ,  $Re_{D_h} = 3985$ ;  $\square$ ,  $Re_{D_h} = 4318$ ;  $\diamond$ ,  $Re_{D_h} = 4835$ ; and solid line, laminar theory [25].

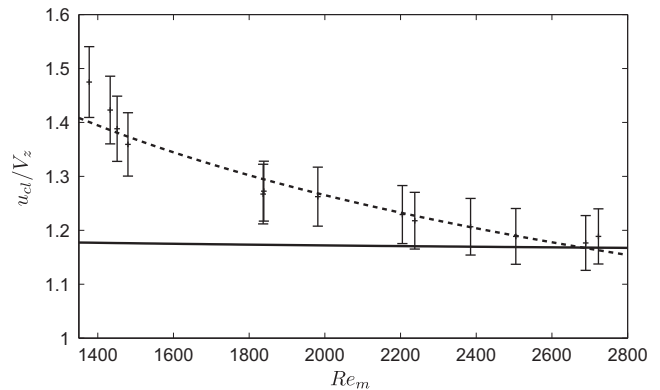


**Fig. 10.** Ratio of centerline velocity to the average velocity as a function of  $Re_m$ . Description: +, experimental data; solid line, Dean's correlation [23],  $u_{cl}/V_z = 1.28Re_m^{-0.0116}$ ; and dashed line,  $u_{cl}/V_z = 10.073Re_m^{-0.273}$ .



$1 \times 10^5$ . Thus, the experimental data for  $1400 < Re_m < 2720$  are higher than predicted by Dean's correlation. Uncertainty in the experimental  $u_{cl}/V_z$  data is approximately 4.35%. Fully turbulent flow is obtained at  $Re_m \approx 2700$  ( $Re_{Dh} \approx 4800$ ) based upon agreement of  $u_{cl}/V_z$  to Dean's correlation. A curve-fit of the experimental  $u_{cl}/V_z$  values, valid over  $1450 < Re_m < 2700$ , is

$$\frac{u_{cl}}{V_z} = 10.0736 Re_m^{-0.273}. \quad (8)$$

Other microchannel studies have reported that fully turbulent flow existed at  $2600 < Re_{Dh} < 3200$  [7–9]. Patel and Head [45], depending upon their criteria, reported that fully turbulent channel flow existed at  $1800 < Re_m < 3000$ . The experimental result for fully turbulent flow of  $Re_m = 2700$  is in agreement with the aforementioned values based upon a correspondence between the measured value of  $u_{cl}/V_z$  and Dean's correlation.

The coefficient of friction for transitional and turbulent flows is presented in Fig. 11 as a function of  $Re_m$  along with its uncertainty, which ranges from 7.8–12.4%. Transition occurs between  $1400 < Re_m < 1460$  based upon a departure from a linear dependence of  $\log(C_f)$  on  $\log(Re_m)$ . The transitional and turbulent  $C_f$  show more scatter than the laminar  $C_f$ . The increased scatter is associated with a lower coefficient of determination value for the linear curve-fit applied to the first five velocity data points in turbulent flow (for all flows, the first five data points correspond to  $y^+ < 5.2$ ). The observed increase in  $C_f$  correlates well with the  $Re_{cr}$  value determined from the mean profile analysis. For the  $Re_m$  investigated, the  $C_f$  data are in relatively good agreement with DNS data at comparable  $Re_m$ , as shown in Fig. 11 [46]. The deviation ranges from 2–8%, with the experimental data slightly lower than the DNS data. While not shown, the trend in the  $C_f$  data obtained by the DNS of Iida and Nagano [47] over  $40 \leq Re_\tau \leq 100$  is also in agreement with the present results. The experimental data fall below Dean's correlation [23],  $C_f = 0.073 Re_m^{-0.25}$ . This discrepancy is likely due to the fact Dean's correlation was based on the range  $Re_m > 6 \times 10^3$ .

### 3.4. Scaling

#### 3.4.1. Inner normalized mean velocity profiles

A quantity is deemed to scale on inner variables,  $v$  and  $u_\tau$ , when its normalized value remains invariant with changes in  $Re_{Dh}$  [24,35]. The inner normalized mean velocity distributions for  $Re_\tau = u_\tau \delta / \nu$  ranging from 58 to 98 are shown in Fig. 12; see Table 2 for equivalent  $Re_{Dh}$ . Note that the inner normalized r.m.s. surface roughness presented in Table 2 is  $\epsilon_{rms}^+ < 1$  for all  $Re_{Dh}$ . For this work,  $Re_\tau$  is based upon the total half channel height, i.e., sum of the half

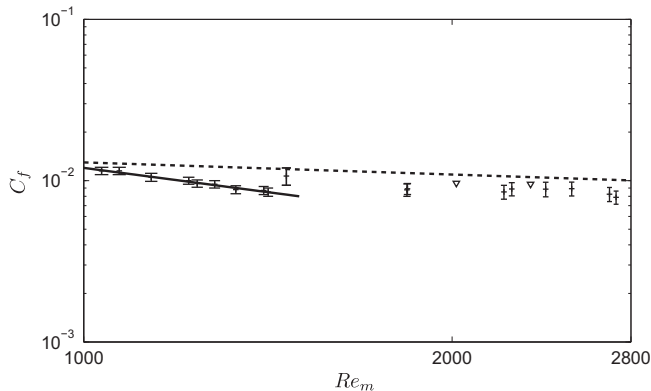


**Fig. 11.** Experimental  $C_f$  compared to macroscale theory and correlations. Description: +, experimental data;  $\nabla$ , DNS data [46]; dashed line, Dean's correlation [23],  $C_f = 0.073 Re_m^{-0.25}$ ; and solid line,  $C_f = 12/Re_m$ .

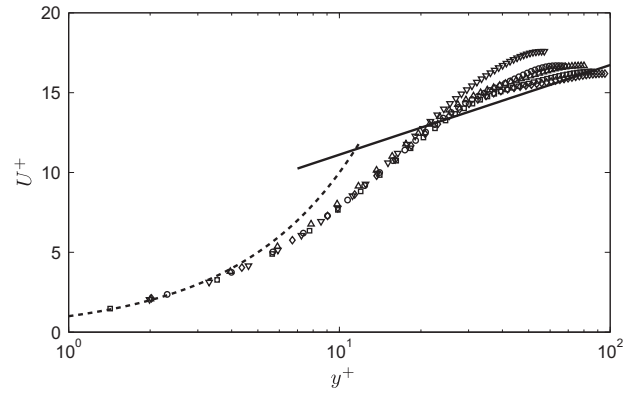


**Fig. 12.** Inner normalized mean velocity profile for  $58 \leq Re_\tau \leq 98$ . Note: Every third data point is shown. Description: dashed line,  $U^+ = y^+$ ; solid line,  $U^+ = (1/0.41) \ln(y^+) + 5.5$ .

channel height used in the MTV analysis and offset distance for the optical access window for the left wall. The friction velocity was obtained from the measured pressure drop and half channel height, which is the height used in the integral analysis; see Table 1 for the dimensions. All profiles presented in this section are for the left wall side (microchannel side where the laser beam enters the test-section). The right wall profiles are of lower quality due to laser beam attenuation, and therefore not presented. For  $y^+ < 20$ , the  $U^+$  data appear to merge to a single curve. As  $Re_\tau$  increases,  $U^+$  rapidly decreases until the profiles adhere much more closely to the log law, with  $\kappa = 0.41$  and  $B = 5.5$ , as shown in Fig. 12. The near merging of the inner normalized mean velocity profiles occurs at  $Re_\tau = 88$ , which is sooner than expected based upon previous experimental evidence [24,35,45]. Note that the profiles take on an increasingly logarithmic-like character through the transitional regime. Based upon the criteria of Harder and Tiederman [48] of having four data points lying on a straight line drawn through  $50 < y^+ < 300$ , no log law exists for the  $Re_\tau$  investigated. The inner normalized mean velocity profiles lack a wake region, which is typical of low  $Re$  flows.

Patel and Head [45] investigated turbulent channel flow over  $1380 < Re_m < 6100$  in a high aspect channel. They reported that for  $Re_m > 3000$ , a logarithmic region existed with constant  $\kappa$  and  $B$ , with values of 0.419 and 5.45, respectively. The data of Patel and Head exhibit a small region of logarithmic dependence for  $Re_m > 3650$ . The trend depicted in Fig. 12 is in excellent agreement with results presented by Patel and Head [45] (although not shown in Fig. 12). Several of the data points presented by Patel and Head were in a  $Re_m$  range similar to the present study ( $1570 < Re_m < 2700$ ). Their  $U^+$  values deviated from the present by  $1 \lesssim \Delta U^+ \lesssim 1.5$ .

The experimental profile for  $Re_\tau = 98$  is also compared to DNS data by Kuroda et al. [49] and Moser et al. [50] at  $Re_\tau$  of 100 and 180. As shown in Fig. 13, the experimental data are in relative agreement for  $y^+ < 40$  and between the two DNS curves for

**Table 2**

Transitional and turbulent friction velocity, Reynolds number, viscous length data, inner normalized r.m.s. surface roughness,  $\epsilon_{rms}^+ = \epsilon_{rms} u_\tau / \nu$ , and symbols used in Figs. 12–17. Note:  $Re_{Dh} = VD_h/\nu$ ,  $Re_m = V_z H_T/\nu$ , and  $Re_\tau = u_\tau \delta/\nu$ .

$Re_\tau$	$Re$	$Re_m$	$u_\tau$ (m/s)	$\nu/u_\tau$ ( $\mu\text{m}$ )	$\epsilon_{rms}^+$	Symbol
58	2894	1480	0.209	4.55	0.13	$\nabla$
70	3410	1839	0.254	3.72	0.15	$\circ$
82	4006	2238	0.292	3.21	0.18	$\triangle$
88	4318	2385	0.314	2.98	0.19	$\square$
98	4800	2689	0.345	2.68	0.21	$\diamond$

$40 < y^+ < 60$ . As previously mentioned, the experimental mean velocity profiles exhibit logarithmic-like behavior sooner than expected, which is verified by the  $Re_\tau = 180$  DNS data. Iida and Nagano [47] performed DNS studies over  $40 \leq Re_\tau \leq 100$ . The present trends for all  $Re_\tau$  are also in agreement with their results, both in trend and magnitude.

#### 3.4.2. Reynolds stress

As discussed in Section 2.5.3, the Reynolds stress is obtained from the mean profile data and the once integrated momentum equation. This evaluation requires the mean wall-normal velocity derivative, which is shown in inner normalized form in Fig. 14. For  $y^+ < 30$ , the trend in the experimental data for  $Re_\tau = 98$  shows deviation from the trend in the DNS data for  $Re_\tau = 100$ . As expected, the inner normalized viscous stress profile steepens through the transitional regime. Over the rest of the cross-section, the trend is as expected, i.e.,  $dU^+/dy^+ \rightarrow 0$  as  $y^+ \rightarrow \delta^+$ .

Inner normalized Reynolds stress data are shown in Fig. 15. As  $Re_\tau$  increases, the magnitude of the peak Reynolds stress increases from 0.307 to 0.563 and the location of the peak in Reynolds stress moves outward in  $y^+$  from 23.6 to 31.3. The results indicate that the peak value of  $\bar{u}v^+$  does not scale on inner variables. Further, if the Reynolds stress is plotted in outer variables, the peak value moves inward (toward the wall) with increasing  $Re_\tau$  and as  $\eta \rightarrow 1$  ( $y^+ \rightarrow \delta^+$ ), the Reynolds stress varies linearly from the peak to the centerline, as shown in Fig. 16. The linear variation in Reynolds stress in the outer region can be derived from classical analyses

of the mean momentum equations [37]. In the near-wall region,  $y^+ < 30$ , the profiles show deviation, which is due to the differences in  $dU^+/dy^+$  values. Consistent with expected trends as  $y^+ \rightarrow 0$ , the  $\bar{u}v^+$  values are approaching zero.

Reynolds stress trends for the microscale experimental results are in good agreement with macroscale high  $Re_\tau$  flows. Inner scaling of the Reynolds stress profiles for macroscale flows does not collapse the profiles, even well into the buffer layer [24,35]. However, Harder and Tiederman [48] reported that the Reynolds stress scaled on inner variables over  $14,430 \leq Re_m \leq 34,640$ . This, however, is a narrow  $Re_m$  band with which to determine the validity of inner scaling since the highest  $Re_m$  is only 2.4 times the lowest  $Re_m$ . The current work also presents data over a narrow  $Re_m$  range, but the Reynolds stress still does not scale on inner variables. This is expected though because flow properties are rapidly evolving with increasing  $Re_{D_h}$  since the flow has just left the laminar regime and the scalings associated with turbulence are not yet established.

For DNS data at  $Re_\tau = 100$ , the peak value of Reynolds stress is 0.587 located at  $y_m^+ = 27$ , where  $y_m^+$  is the peak location in Reynolds stress [49]. For the experimental data at  $Re_\tau = 98$ , the peak location is  $y_m^+ = 31.3$  and the peak Reynolds stress value is 0.563, however, these values are in relatively good agreement with the DNS data. For  $y^+ > 35$ , the experimental Reynolds stress values are nearly equal to those for the DNS results at  $Re_\tau = 100$ . Sreenivasan [51] and later Sreenivasan and Sahay [52] showed that  $y_m^+ \propto \delta^{+0.5}$  with the constant of proportionality being about 2. Wei et al. [53] fur-

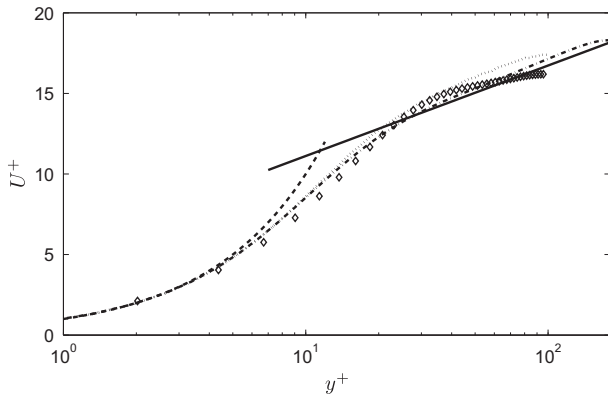


**Fig. 13.** Inner normalized mean velocity profile with DNS comparison. Note: Every third data point is shown. Description: dashed line,  $U^+ = y^+$ ; solid line,  $U^+ = (1/0.41)\ln(y^+) + 5.5$ ; dotted line, DNS data at  $Re_\tau = 100$  [49]; dash-dot line, DNS data at  $Re_\tau = 180$  [50].

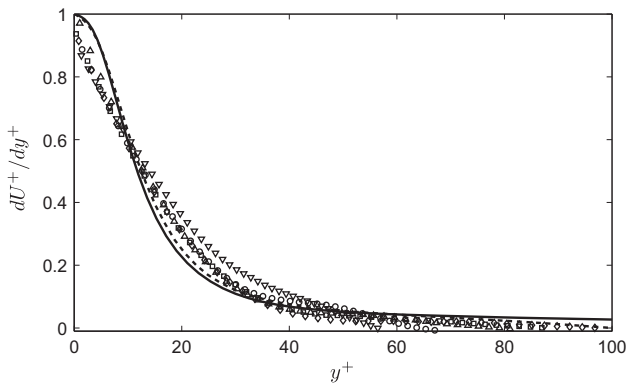


**Fig. 14.** Mean wall-normal inner normalized velocity gradient at various  $Re_\tau$ . Note: Every third data point is shown. Description: dashed line, DNS data at  $Re_\tau = 100$  [49]; solid line, DNS data at  $Re_\tau = 180$  [50].

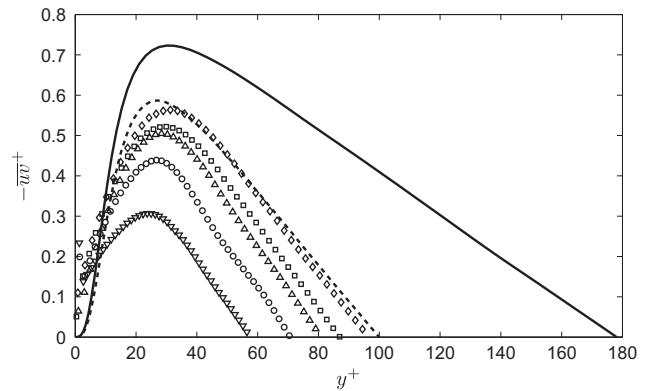


**Fig. 15.** Inner normalized Reynolds stress obtained from the once integrated momentum equation along with DNS data. Note: Every third data point is shown. Description: dashed line, DNS data at  $Re_\tau = 100$  [49]; solid line, DNS data at  $Re_\tau = 180$  [50].

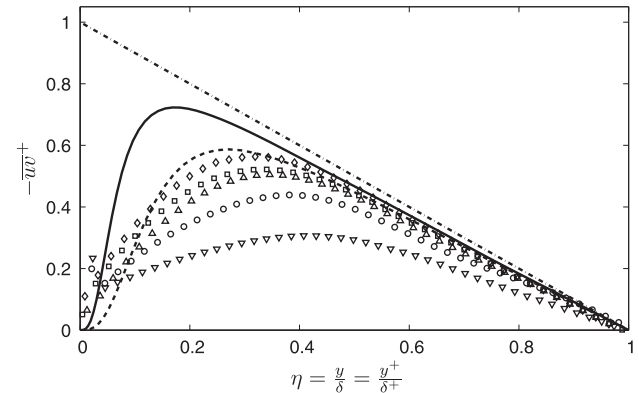


**Fig. 16.** Reynolds stress profiles in wall units as a function of outer variables. Note: Every third data point is shown. Description: dashed line, DNS data at  $Re_\tau = 100$  [49]; solid line, DNS data at  $Re_\tau = 180$  [50]; dash-dot line,  $1 - \eta$ .

ther verified this result empirically and via analysis of the momentum equations directly. For this work, a curve-fit with the same power fit form resulted in  $y_m^+ = 3.1\delta^{+0.502}$ . The deviation for the present experimental work in comparison to theory is due to the Reynolds stress peak not occurring inside the log law regime. Although the slope constant is different at high  $Re_{D_h}$ , it is interesting that the  $-\overline{uv}^+$  peak still shifts outward at a  $\delta^{+1/2}$  rate.

### 3.4.3. Turbulence production

For fully developed channel flow, the production term in the turbulence kinetic energy equation reduces to  $-\overline{uv}dU/dy$ . The turbulent energy production profiles are obtained by taking the product of the calculated Reynolds stress,  $-\overline{uv}^+$ , from the once integrated momentum balance and the mean velocity gradient,  $dU^+/dy^+$ , at the same  $y^+$  location. The inner normalized production of mean turbulent kinetic energy,  $P^+$ , is shown in Fig. 17. As  $Re_\tau$  increases, the maximum  $P^+$  value increases, which is consistent with the Reynolds and viscous stress trends. The location of peak production ranges from  $y_p^+ = 10.6$  to 12.9, which is in excellent agreement with macroscale values of  $y_p^+ = 12$ , where  $y_p^+$  is the peak production location [24,35,54]. DNS results presented by Tsukahara et al. [46] indicate, however, that the production peak in inner variables moves slightly towards the wall with  $Re_\tau$  over  $70 < Re_\tau < 180$ , with the peak occurring at  $y_p^+ \approx 15$  for  $Re_\tau = 70$  and  $y_p^+ = 11$  for  $Re_\tau = 180$ . The experimental results also indicate that  $P^+$  does not scale on inner variables. This is consistent with DNS findings [46] and experimental results [24]. It is well known that as  $\delta^+$  approaches infinity, the maximum production value is 0.25 [24]. Therefore, with increasing  $Re_\tau$ , the peak production increases asymptotically, which is shown in Fig. 17. The maximum value for  $Re_\tau = 98$  at  $y_p^+ = 12.0$  is  $P_{max}^+ = 0.185$ , which is in agreement with the DNS results at  $Re_\tau = 100$  ( $P_{max}^+ = 0.188$  at  $y_p^+ = 13.4$ ) [49]. It can be shown for finite  $\delta^+$  [46], that the peak production value is

$$P_{max}^+ = \frac{1}{4} \left( 1 - \frac{y_p^+}{\delta^+} \right)^2. \quad (9)$$

Substituting the experimental  $y_p^+$  into Eq. (9), the predicted  $P_{max}^+$  values are 4–25% higher than the experimental values, with the highest deviation at  $\delta^+ = 58$ .

The location of Reynolds and viscous stress equality provides information on the relative significance of the two stresses. As presented in Table 3, the  $y^+$  location where the Reynolds and viscous stress are equal moves towards the wall for increasing  $Re_\tau$ . For  $Re_\tau = 58$ , the value and location where  $-\overline{uv}^+ = dU^+/dy^+ = 0.305$  is at  $y^+ = 22.5$ , and for  $Re_\tau = 98$ ,  $-\overline{uv}^+ = dU^+/dy^+ = 0.434$  at  $y^+ = 14.9$ . The progression towards the wall is due to the rapid increase in Reynolds stress in the near-wall region with increasing

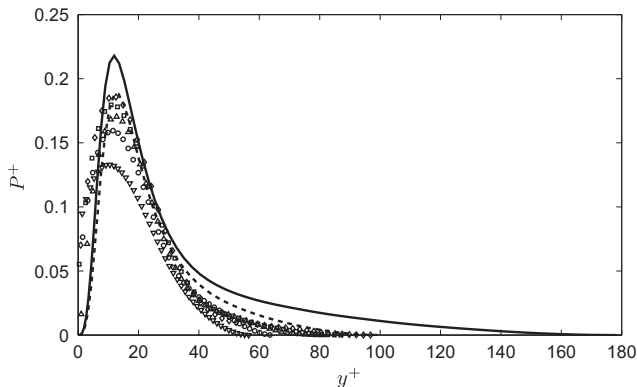


**Fig. 17.** Inner normalized production of turbulent kinetic energy. Note: Every third data point is shown. Description: dashed line, DNS data at  $Re_\tau = 100$  [49]; solid line, DNS data at  $Re_\tau = 180$  [50].

**Table 3**

Summary of the  $y^+$  location where the viscous stress equals the Reynolds stress.

$Re_\tau$	Method	$y^+$	$-\overline{uv}^+ = dU^+/dy^+$
58	Exp.	22.5	0.305
70	Exp.	17.4	0.383
82	Exp.	16.0	0.409
88	Exp.	15.3	0.421
98	Exp.	14.9	0.434
100	DNS	14.1	0.430
180	DNS	12.4	0.466

$Re_\tau$ . It can be shown for large  $\delta^+$  that the stress terms are equivalent when both equal  $1/2$  [44]. Here, the value of equivalent Reynolds and viscous stresses approaches 0.5 asymptotically as  $Re_\tau$  increases, as indicated by Table 3. Even at low  $Re_\tau$ , the Reynolds and viscous stress are equal at a  $y^+$  location inside the buffer layer ( $5 < y^+ < 30$ ).

## 4. Conclusion

An experimental study of water flows through a high aspect ratio microchannel was undertaken to examine the validity of macroscale theory and correlations at the microscale and to investigate local laminar, transitional, and turbulent flow characteristics. MTV was used to obtain mean spatially resolved velocity profiles for laminar, transitional, and turbulent flows over  $173 \leq Re_{D_h} \leq 4830$ . Also, for the first time in microchannel flow, inner scaling of transitional and turbulent velocity profiles was experimentally investigated.

The laminar velocimetry data and coefficient of friction were in excellent agreement with macroscale theory. Transition from laminar flow, based upon a change in dimensionless velocity profile shape occurs at  $Re_{D_h} \approx 2800$ . This transitional  $Re_{D_h}$  was in excellent agreement with pressure drop results, which were based upon a deviation from a linear dependence of  $\log(f)$  on  $\log(Re_{D_h})$ . Based upon  $Re_m$ , transition occurs at  $Re_m \approx 1400$ . Fully developed turbulent flow is found to exist at  $Re_m \approx 2700$  ( $Re_{D_h} \approx 4800$ ) based upon a correspondence of  $u_{cl}/V_z$  to Dean's correlation. In the transitional and turbulent regimes, inner normalized mean velocity profiles scale up to  $y^+ = 20$ , whereas the Reynolds stress and production profiles exhibit features that do not scale on inner variables. The inner normalized mean velocity profiles become increasing log-like through the transitional regime. Even though the Reynolds stress and production of turbulent kinetic energy are derived data, the agreement between the peak location of the Reynolds stress scaling  $y_m^+ \propto \delta^{+0.502}$  and the location of the peak production,  $y_p^+ \approx 11.8$ , are in excellent agreement with macroscale data. The experimental trends for the inner normalized mean velocity, Reynolds stress, and production are in agreement with macroscale experimental and DNS data. Based upon experimental and DNS macroscale data and trends, one can conclude that microscale turbulent flows are statistically similar.

At this scale, it can be concluded that no microscale effect exists that alters either the laminar or turbulent transport of momentum. Therefore, macroscale theory and correlations can be used to design microfluidic devices. In addition, microscale transitional/turbulent flows exhibit distinct statistical similarities to macroscale flows. Furthermore, in contrast to microscale PIV studies to date, the present effort demonstrates that MTV can obtain a well-resolved profile well into the near-wall region.

## Acknowledgement

This study was supported by NSF IGERT Grant DGE 9987616. The experiments documented herein comply with the current laws of the United States.

## References

- [1] H. Stone, A. Stroock, A. Ajdari, Engineering flows in small devices: microfluidics toward a lab-on-a-chip, *Annual Review of Fluid Mechanics* 36 (2004) 381–411.
- [2] C.M. Ho, Y.C. Tai, Micro-electro-mechanical-systems (MEMS) and fluid flows, *Annual Review of Fluid Mechanics* 30 (1998) 579–612.
- [3] M. Gad el Hak, The fluid mechanics of microdevices – the Freeman scholar lecture, *Journal of Fluids Engineering* 121 (1999) 5–33.
- [4] W.R. Lempert, N. Jiang, S. Sethuram, M. Samimy, Molecular tagging velocimetry measurements in supersonic microjets, *AIAA* 40 (2002) 1065–1070.
- [5] D. Tuckerman, R. Pease, High-performance heat sinking for VLSI, *IEEE Electron Device Letters* 2 (1981) 126–129.
- [6] K.V. Sharp, R.J. Adrian, Transition from laminar to turbulent flow in liquid filled microtubes, *Experiments in Fluids* 36 (2004) 741–747.
- [7] H. Li, R. Ewaldt, M.G. Olsen, Turbulent and transitional velocity measurements in a rectangular microchannel using microscopic particle image velocimetry, *Experimental Thermal and Fluid Science* 29 (2005) 435–446.
- [8] H. Li, M.G. Olsen, Aspect ratio effects on turbulent and transitional flow in rectangular microchannels as measured with micro PIV, *Journal of Fluids Engineering* 128 (2006) 305–315.
- [9] H. Li, M.G. Olsen, MicroPIV measurements of turbulent flow in square microchannels with hydraulic diameters from 200  $\mu\text{m}$  to 640  $\mu\text{m}$ , *International Journal of Heat and Fluid Flow* 27 (2006) 123–134.
- [10] H. Li, M.G. Olsen, Examination of large-scale structures in turbulent microchannel flow, *Experiments in Fluids* 40 (2006) 733–743.
- [11] V. Natrajan, K. Christensen, Microscopic particle image velocimetry measurements of transition to turbulence in microscale capillaries, *Experiments in Fluids* 43 (2007) 1–16.
- [12] V. Natrajan, E. Yamaguchi, K. Christensen, Statistical and structural similarities between micro- and macroscale wall turbulence, *Microfluid Nanofluid* 3 (2007) 89–100.
- [13] M. Koochesfahani, R. Cohn, C. MacKinnon, Simultaneous whole-field measurements of velocity and concentration fields using combination of MTV and LIF, *Measurement Science and Technology* 11 (2000) 1289–1300.
- [14] M.M. Koochesfahani, R. Cohn, C.P. Gendrich, D.G. Nocera, Molecular tagging diagnostics for the study of kinematics and mixing in liquid phase flows, *Developments in Laser Techniques and Fluid Mechanics: Selected Papers from the 8th International Symposium, Lisbon, Portugal, Springer-Verlag, Berlin, Heidelberg, 1997*.
- [15] R. Sadr, J.C. Klewicki, An experimental investigation of the near-field flow development in coaxial jets, *Physics of Fluids* 15 (2003) 1233–1246.
- [16] M.M. Koochesfahani, D.G. Nocera, Molecular Tagging Velocimetry, in: *Handbook of Experimental Fluid Dynamics*, Springer, 2007 (Chapter 5.4).
- [17] D. Maynes, A. Webb, Velocity profile characterization in sub-millimeter diameter tubes using molecular tagging velocimetry, *Experiments in Fluids* 32 (2002) 3–15.
- [18] R.B. Hill, J.C. Klewicki, Data reduction methods for flow tagging velocity measurements, *Experiments in Fluids* 20 (1996) 142–152.
- [19] C.P. Gendrich, M.M. Koochesfahani, A spatial correlation technique for estimating velocity fields using molecular tagging velocimetry (MTV), *Experiments in Fluids* 22 (1996) 67–77.
- [20] B. Thompson, D. Maynes, B. Webb, Micro-scale velocity measurements using molecular tagging velocimetry: methodology and uncertainty, *ASME Fluids Engineering Division Summer Meeting*, 2002, pp. 123–133.
- [21] B. Thompson, D. Maynes, B. Webb, Characterization of the hydrodynamically developing flow in a microtube using MTV, *Journal of Fluids Engineering* 127 (2005) 1003–1012.
- [22] C.L. Lum, An experimental study of pressure- and electroosmotically-driven flows in microchannels with surface modifications, Ph.D. Thesis, Michigan State University, 2005.
- [23] R.B. Dean, Reynolds number dependence of skin friction and other bulk flow variables in two-dimensional rectangular duct flow, *Journal of Fluids Engineering* 100 (1978) 215–223.
- [24] T. Wei, W.W. Willmarth, Reynolds-number effects on the structure of a turbulent channel flow, *Journal of Fluid Mechanics* 204 (1989) 57–95.
- [25] R. Shah, A. London, *Laminar Flow Forced Convection in Ducts*, Academic Press, 1978.
- [26] D. Costaschuk, J.R. Elsnab, S.J. Petersen, J.C. Klewicki, T.A. Ameel, Axial static pressure measurements of water flow in a rectangular microchannel, *Experiments in Fluids* 43 (2007) 907–916.
- [27] K. Lien, J.P. Monty, M.S. Chong, A. Ooi, The entrance length for fully developed turbulent channel flow, in: *15th Australasian Fluid Mechanics Conference*, 2004.
- [28] H. Coleman, W.G. Steele, *Experimentation and Uncertainty Analysis for Engineers*, second ed., John Wiley & Sons, 1999.
- [29] A. Ponce, P.A. Wong, J.J. Way, D.G. Nocera, Intense phosphorescence triggered by alcohols upon formation of a cyclodextrin ternary complex, *Journal Physical Chemistry* 97 (1993) 11137–11142.
- [30] C.P. Gendrich, M.M. Koochesfahani, D.G. Nocera, Molecular tagging velocimetry and other novel applications of a new phosphorescent supramolecule, *Experiments in Fluids* 23 (1997) 361–372.
- [31] A. Savitzky, M.J. Golay, Smoothing and differentiation of data by simplified least squares procedures, *Analytical Chemistry* 36 (1964) 1627–1639.
- [32] E.M. Thurlow, J.C. Klewicki, Experimental study of turbulent Poiseuille–Couette flow, *Physics of Fluids* 12 (2000) 865–875.
- [33] R.J. Moffat, Describing the uncertainties in experimental results, *Experimental Thermal and Fluid Science* 1 (1988) 3–17.
- [34] S. Chapra, R. Canale, *Numerical Methods for Engineers*, 3rd ed., McGraw-Hill, 1998.
- [35] M. Gad el Hak, P.R. Bandyopadhyay, Reynolds number effects in wall-bounded turbulent flows, *Applied Mechanics Review* 47 (1994) 307–365.
- [36] R.L. Panton, *Incompressible Flows*, second ed., John Wiley & Sons, 1996.
- [37] H. Tennekes, J.L. Lumley, *A First Course in Turbulence*, The MIT Press, 1972.
- [38] R.W. Fox, A.T. McDonald, *Introduction to Fluid Mechanics*, fifth ed., John Wiley & Sons, Inc., 1998.
- [39] R.W. Hyland, A. Wexler, Formulations for the thermodynamic properties of the saturated phases of H<sub>2</sub>O from 173.15 K to 473.15 K, Technical Report RP 216, Part 1, ASHRAE, 1980.
- [40] A. Nagashima, Viscosity of water substances – new international formulation and its background, *Journal Physical Chemical Reference Data* 1959 (1977).
- [41] J.R. Elsnab, Mean velocity profiles in a high aspect microchannel, Ph.D. Thesis, University of Utah, 2008.
- [42] S. Haaland, Simple and explicit formulas for the friction factor in turbulent pipe flow, *Journal Fluid Engineering* (1983) 89–90.
- [43] J. Judy, D. Maynes, B. Webb, Characterization of frictional pressure drop for liquid flows through a microchannels, *International Journal of Heat and Mass Transfer* 45 (2002) 3477–3489.
- [44] S.B. Pope, *Turbulent Flows*, Cambridge, 2000.
- [45] V.C. Patel, M.R. Head, Some observations on skin friction and velocity profiles in fully developed pipe and channel flows, *Journal of Fluid Mechanics* (1969) 181–201.
- [46] T. Tsukahara, Y. Seki, H. Kawamura, D. Tochio, DNS of turbulent channel flow with very low Reynolds numbers, in: *WCCM VI in Conjunction with APCOM'04*, September 5–10, 2004, Tsinghua University Press & Springer-Verlag, Beijing, China, 2004.
- [47] O. Iida, Y. Nagano, The relaminarization mechanisms of turbulent channel flow at low Reynolds numbers, *Flow, Turbulence and Combustion* 60 (1998) 193–213.
- [48] K.J. Harder, W.G. Tiederman, Drag reduction and turbulent structure in two-dimensional channel flows, *Philosophical Transactions: Physical Sciences and Engineering* 336 (1991) 19–34.
- [49] A. Kuroda, N. Kasagi, M. Hirata, A direct numerical simulation of the fully developed turbulent channel flow, in: *International Symposium on Computational Fluid Dynamics*, Nagoya, Japan, 1989, pp. 1174–1179.
- [50] R.B. Moser, J. Kim, N.N. Mansour, Direct numerical simulation of turbulent channel flow up to  $Re_\tau = 590$ , *Physics of Fluids* 11 (1999) 943–945.
- [51] K.R. Sreenivasan, The turbulent boundary layer, in: *Frontiers in Experimental Fluid Mechanics*, Springer-Verlag, 1989.
- [52] K.R. Sreenivasan, A. Sahay, The persistence of viscous effects in the overlap region, and the mean velocity in turbulent pipe and channel flows, in: *Self-Sustaining Mechanisms of Wall Turbulence*, Computational Mechanics Publications, 1997.
- [53] T. Wei, P. Fife, J.C. Klewicki, P. McMurtry, Properties of the mean momentum balance in turbulent boundary layer, pipe and channel flows, *Journal of Fluid Mechanics* 522 (2005) 303–327.
- [54] J. Kim, P. Moin, R. Moser, Turbulence statistics in fully developed channel flow at low Reynolds number, *Journal of Fluid Mechanics* 177 (1987) 133–166.